

*Original Research*

# Investigation of Water Spraying Distribution by Multi-points Characterization System in Simulation Tunnel

Wei Lu<sup>1\*</sup>, Xiaoping Ouyang<sup>2</sup>, Wenjun Zhu<sup>3</sup>

<sup>1</sup>Foshan Green Intelligent Manufacturing Research Institute of Xiangtan University, Foshan 528399, Guangdong, PR China

<sup>2</sup>Northwest Institute of Nuclear Technology, Xi'an 710000, Shanxi, PR China

<sup>3</sup>National Key Laboratory of Shock Wave and Detonation Physics, Institute of Fluid Physics, China Academy of Engineering Physics, Mianyang 621900, Sichuan, PR China

*Received: 6 July 2022*

*Accepted: 17 August 2022*

## Abstract

Water spraying is widely used in dust reduction of coal mines. A set of dust governance system urgently requires spray effects and its characteristics. A spray distribution characterization system is invented in this study. With CFD calculation results, the spray droplet size and concentration are measured by this characterization system at speed 0.5, 1, 1.5 and 2 m/s in a simulation tunnel. The results demonstrate that the droplet size reaches 5.416  $\mu\text{m}$  through particle collision and evaporation. From 5 m to 30 m, the spray concentration decreases to the fluctuation valley at 15 m and picks up again, whereas the condition varies at the speed of 0.5 m/s. This study provides additional insights for spray characterization and supports the spray dust reduction.

**Keywords:** spray dust reduction, spray distribution characterization, CFD, droplet size, spray concentration

## Introduction

High dust hazard produced in coal mining process not only can threaten miners' health and influence working efficiency, especially the respiratory dust, but also cause dust explosion [1-4]. By 2016, 27992 cases of occupational pneumoconiosis from 31789 cases of occupational disease have been reported and 95.49% of which are from coal miners [5]. Therefore, for

ensuring the normal working and the health of workers, an effective dust reduction technology is in urgent need. Among all the dust reduction technologies, e.g., ventilation, dust remover, spray dust fall, foam dust removal, individual protection, of which the spray dust fall method is the most extensively applied for its advantages of economy, simplicity and practicability [6-9]. The principle of aerodynamics shows that the cloud-fog particles can catch the respirable dust of similar particle size more effectively [10-12]. Some works have revealed the importance of spray characteristics to the typical water-based dust reduction by studying the influences from different spray media [13-14].

---

\*e-mail: carol\_luwei@163.com

For improving the efficiency of dust fall, spray distribution in tunnel by nozzles layout is crucial for spray dust fall exploring.

To study the spray distribution, a detection system of spray particle size and concentration has been investigated. About the detection of water-fog particle size [15-19], the Laser Particle Sizer based on laser scattering technology by using logarithmic distribution method for data analysis and processing is widely used in laboratories [20, 21]. Due to the laser distance and penetration limitation, with the practical consideration, the Laser Particle Sizer is not suitable for the experimental tunnel. In the present work, the invention with detection method and its devices has been designed for simultaneously characterizing the size and concentration of water fog for multi-points in large space. This method is based on oil pool sampling and a new set of particle collector. Firstly, each value of water-fog particle size and concentration in experiments is obtained. The characteristics of water fog in the monitoring area are analyzed secondly. Here the particle size analysis result of the detection point 10 m from the spray zone, under the wind speed of 1.0 m/s, is compared with the particle size result of a single two-phase atomizing nozzle detected by the Laser Particle Sizer, which verified the validity of the method. Before applying this method into experiments, the spray flow field is simulated and analyzed by numerical simulation software, according to that a preliminary understanding of the flow mode in the experimental tunnel can provide a good reference for the arrangement of experimental sampling devices. With the condition that the pressure air flow is input into the spray flow field and their interaction, the flow velocity changing discipline can guide the analysis of the pressure air

flow field, the movement of water-fog particles and the space parameters. And the discrete phase is added into the model to simulate the migration and distribution of water-fog particles under varied conditions of pressure air. The post-treatment result graphs are obtained to guide and analyze the experimental phenomenon combined with the experimental results. The spray spreading disciplines in simulated tunnel has been revealed, and the precision-improving points of this method are also analyzed.

## Methods and Experiments

### Detection System

#### *Particulate Collector*

The particulate collector mainly contains the collector head and the support as shown in Fig. 1. The height of sampling piece has been adjusted to the respiratory zone for experiments. The collector uses the negative pressure fan to generate negative pressure in the collector head, and the air flow around the air inlet of the collector head is sucked in. The fine particles in the air flow are intercepted by the sampling piece placed on the center of the sampling plate, and the sealing medium in the sampling piece will seal the fine particles timely.

#### *Particle Size Analysis Method*

In the process of particle detection, the metallographic microscope images the sample piece with fine particles online firstly. The micro particle

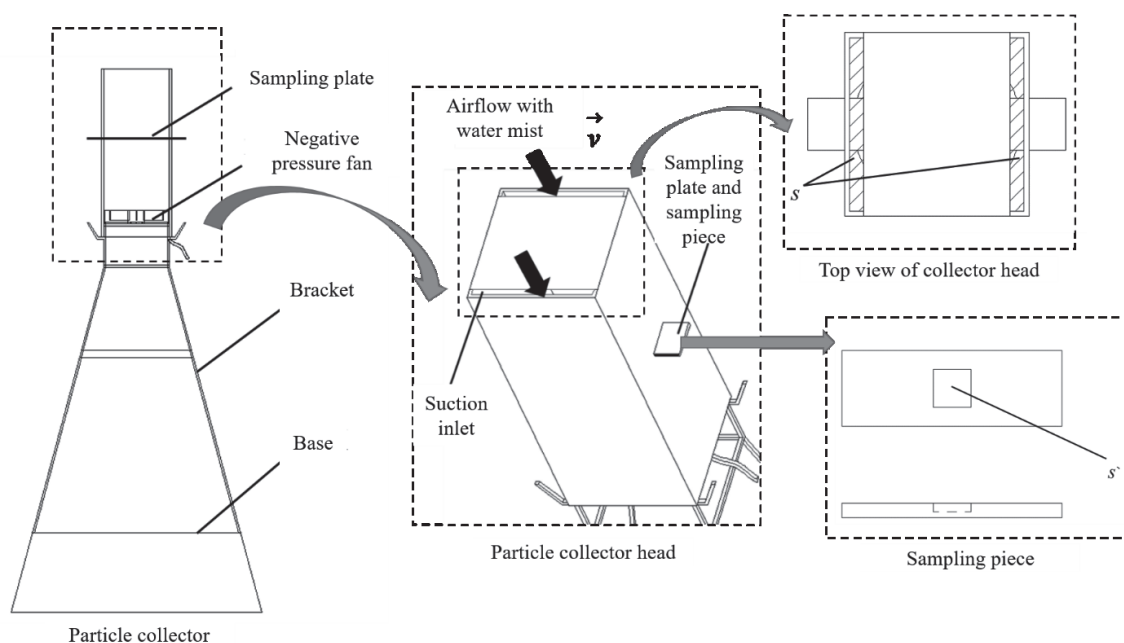


Fig. 1. Particle collector.

sizes in the image are measured by software, and the particles information are counted secondly. Thirdly the particle size and concentration analysis method is used for calculation. Furthermore, the values of observation times for each water-fog particle sample are obtained by the ratio of the concave pool area of the sampling piece to the image area.

After metallographic microscope imaging, the image area is expressed by:

$$s'' = 659.65 \times 494.11 \approx 325939.66 \mu\text{m}^2 \quad (1)$$

The amount of samples to be tested is given by the following expression:

$$n = \frac{s'}{s'' \times 10^{-6}} \quad (2)$$

where  $s'$  represents the concave pool area of the sample piece, as shown in Fig. 1.  $s''$  represents the image area from metallographic microscope.

The area of the sample cell is 169 mm<sup>2</sup> through calculation, so the actual value  $n$  of each sample piece by software is counted as 519. The water-fog particles are evenly distributed in the sampling film, so the particle size value of each experimental point is approximately the median diameter D50, which means the number of particles is smaller than this diameter account for 50% of all particles. The D50 is calculated from the measured data in images that are detected 3 times per sample piece at lowest.

#### Particle Concentration Analysis Method

The wind speed  $v$  at the air inlet of the particle collector in Fig. 1 is measured by a wind speed detector. So the movement height  $h$  of the airflow within the sampling time  $t$  can be obtained. The effective suction cross-sectional area  $s$  of the collection head is shown in Fig. 1. The total volume in time  $t$  of the airflow passing through the collector head is the product of  $h$  and  $s$ . The ratio of the air flow volume with water-fog particles flowing through the concave pool to the total air flow volume entering the collector head, is equal to the ratio of the concave pool area of the sampling piece to the cross-sectional area of the collector head. 519 times of the average value of the three waterfog volumes from 3 effective images, which is the total volume  $V$  of water fog flowing through the concave pool. The ratio of the mass of water-fog particles flowing through the concave pool to the volume of airflow flowing through the concave pool, which is the mass concentration of waterfog particles in the space where the collection point is located.

Mass concentration of water-fog particles is expressed by:

$$\rho_n = \frac{m}{V'} = \frac{V \times 10^6}{V'} \quad (3)$$

where  $m$  represents the mass of water-fog particles flowing through the concave pool of sampling piece;  $V'$  is the volume of air flow with water-fog particles flowing through the concave pool of the sampling piece.

Volume of water-fog particles flowing through the concave pool of sampling piece is given by:

$$V = (s' / s'') \times \frac{(V_1 + V_2 + V_3)}{3} \quad (4)$$

where  $V_1$ ,  $V_2$ ,  $V_3$  represent the volume of water-fog particles in an observation image in the concave pool of the sampling plate.

The volume of water-fog particles in an observation image is expressed by:

$$V_i = \frac{4}{3} \pi (r_1^3 n_1 + r_2^3 n_2 + r_3^3 n_3 + \dots) \quad (5)$$

where  $r_1$ ,  $r_2$ ,  $r_3$  et al. represent the radius of water-fog particles in the observed image, and  $n_1$ ,  $n_2$ ,  $n_3$  et al. represent the amount of corresponding water-fog particle size.

Volume of air flow with water-fog particles flowing through the concave pool of sampling piece is expressed by:

$$V' = h \times s \times \frac{s'}{100 \times 100} \quad (6)$$

where  $s'$  represents the area of concave pool.

#### Distribution Simulation of Cloud-Fog Particles Size and Concentration

Ahead of the spray detection in experimental tunnel, the numerical simulation calculations have been done in fluid exploring with CFD software-ANSYS Fluent [22-26]. Here a series of flow simulation by DPM model have been calculated in different speed values. Discrete particle model calculates the particle phase as discrete phase [27]. DPM takes full account of the interaction between gas and particle phases and assumes no diffusion of particle phase in orbit. The governing equations of DPM include continuity equation, momentum equation and energy equation of gas phase and particle phase as shown in Table 1. For incompressible Newtonian fluid, the continuous phase conforms to the conservation of mass and momentum, and the N-S equation during calculation. To the model solution equation, the Euler-Lagrange model is used when particle phase is added. The gas phase is represented by continuous Euler coordinate system [28]. The particle phase is represented by discrete Lagrange

Table 1. Governing equations of DPM.

	Gas phase	Particle phase
Continuity equation	$\frac{\partial \rho}{\partial t} + \frac{\partial}{\partial x}(\rho_g v_{gx}) + \frac{\partial}{\partial y}(\rho_g v_{gy}) + \frac{\partial}{\partial z}(\rho_g v_{gz}) = S$	$\frac{\partial \rho_{pK}}{\partial t} + \frac{\partial}{\partial x}(\rho_{pK} v_{pKx}) + \frac{\partial}{\partial y}(\rho_{pK} v_{pKy}) + \frac{\partial}{\partial z}(\rho_{pK} v_{pKz}) = S_{pK}$
Momentum equation	$\begin{aligned} &\frac{\partial}{\partial t}(\rho_g v_{gx}) + \frac{\partial}{\partial x}(\rho_g v_{gx} v_{gx}) + \frac{\partial}{\partial y}(\rho_g v_{gy} v_{gx}) + \frac{\partial}{\partial z}(\rho_g v_{gz} v_{gx}) = \\ &-\frac{\partial p_g}{\partial x} + \frac{\partial}{\partial x} \tau_{gxx} + \frac{\partial}{\partial y} \tau_{gxy} + \frac{\partial}{\partial z} \tau_{gzx} \\ &+ \rho_g F_{gx} + \sum_K F_{gpKx} + v_{gx} S \end{aligned}$	$\begin{aligned} &\frac{\partial}{\partial t}(\rho_{pK} v_{pKx}) + \frac{\partial}{\partial x}(\rho_{pK} v_{gx} v_{pKx}) + \frac{\partial}{\partial y}(\rho_{pK} v_{gy} v_{pKx}) + \frac{\partial}{\partial z}(\rho_{pK} v_{gz} v_{pKx}) = \\ &-\frac{\partial p_{pK}}{\partial x} + \frac{\partial}{\partial x} \tau_{pKxx} + \frac{\partial}{\partial y} \tau_{pKyx} + \frac{\partial}{\partial z} \tau_{pKzx} \\ &+ \rho_{pK} F_{pKx} + J_{pKx} + v_{gx} S_{pK} \end{aligned}$
Energy equation	$\begin{aligned} &\frac{\partial}{\partial t}(\rho_g c_{pg} T_g) + \frac{\partial}{\partial x}(\rho_g v_{gx} c_{pg} T_g) \\ &-\frac{\partial p_g}{\partial t} = \frac{\partial p_g}{\partial t} (\lambda_g \frac{\partial T_g}{\partial x}) + \\ &S c_{pg} T_g - \sum_K n_{pK} Q_K - Q_{rg} \end{aligned}$	$\begin{aligned} &\frac{\partial}{\partial t}(\rho_{pK} c_{pK} T_{pK}) + \frac{\partial}{\partial x}(\rho_{pK} v_{pKx} c_{pK} T_{pK}) = \\ &\frac{\partial}{\partial t} (\lambda_{pK} \frac{\partial T_{pK}}{\partial x}) + S_{pK} c_{pg} T_g + n_{pK} (Q_K - Q_{rK}) \end{aligned}$

where  $Q_K$  is the heat removed from the fluid by the K term particles due to convective heat transfer;  $J_{pK}$  is the component force of the K - term particle diffusion flow;  $F_{gpK}$  is the resultant force of the particle on the fluid phase; subscript g represents gas phase; subscript p represents particle phase; K represents K particle phase.

coordinate system. In the calculation of two-phase flow field, the particle phase as the velocity vector can ensure the randomness of particle movement. According to the experimental tunnel structure and flow field

conditions, the model has been modeled in the pre-processing software. After iterative calculation, particle movement information are observed in post-processing analysis.

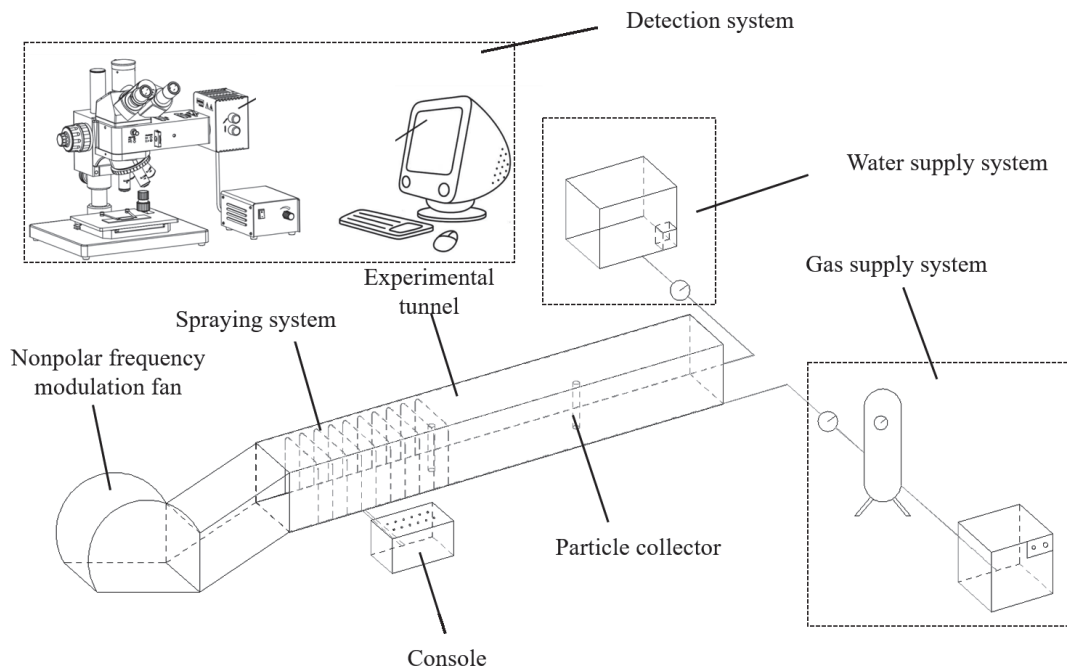


Fig. 2. Experimental system layout.

### Experimental Working Process and System Composition

The water pressure and air pressure has been adjusted well firstly in the experimental tunnel. The two-phase nozzles spraying system have been checked secondly. After that, 9 detection points are set in the experimental tunnel. The no. 1 detection point is at the end of the spray area. The no. 2 detection point is at 5 m distance from the no. 1 detection point, and the distance between each collection point is 5 m. The sealed medium has been instilled into the concave pool of each particle collector already. The experimental temperature and humidity also have been recorded. After 3 min spraying, the distribution of the water-fog particles in the experimental tunnel is basically stable. The particle collector obtains the surrounding water particles. After 2 min, the particle collector is closed firstly, and secondly the two-phase flow spray system is closed. Thirdly, the sampling pieces are removed for detection. According to the calculation method of particle size and concentration, the data of each sampling point are obtained and analyzed.

The experimental system group includes four parts, i.e., spraying, particle acquisition, particle detection and data analysis, as shown in Fig. 2. The spray particle size is 10.0  $\mu\text{m}$  in average, and the pressure of supplying gas is 0.1 MPa  $\sim$  0.3 MPa, with the flow rate of the gas supply is 30.0 L/min  $\sim$  40.0 L/min. The water supply

pressure is 0.1 MPa  $\sim$  0.3 MPa. And the water supply flow rate is 2 kg/h  $\sim$  5 kg/h. 10 rows of nozzles are set in spraying system, and 8 nozzles each series in row.

## Results and Discussion

### Experimental Verification

After sampling at 10 m from the spray zone at 1.0 m/s wind speed, the particle sizes are measured by metallographic microscope and software. The 3 regions are randomly selected within the observation range of the concave pool of the sampling piece, and the measurement results are shown in Fig. 3.

The data arrangement of water-fog particles in Fig. 3 is shown in Table 2. The average water-fog particle size in the sampling point area is 7.06  $\mu\text{m}$ , corresponding to the median diameter D50 value of particle count, and the particle size distribution is shown in Fig. 4.

Through the measurement, the wind speed  $v$  of the particle collector is 2.453 m/s, and the collection time  $t$  is 3 min. The statistics of particle size data in Fig. 3 are shown in Table 3, and the number of corresponding particle sizes is shown in Table 4.

The volume  $V'$  is calculated as 0.007  $\text{m}^3$ . The corresponding volumes of water-fog particles in 3 detection areas of the sampling image are calculated as 3526.96  $\mu\text{m}^3$ , 4635.30  $\mu\text{m}^3$ , 3722.99  $\mu\text{m}^3$ . The volume

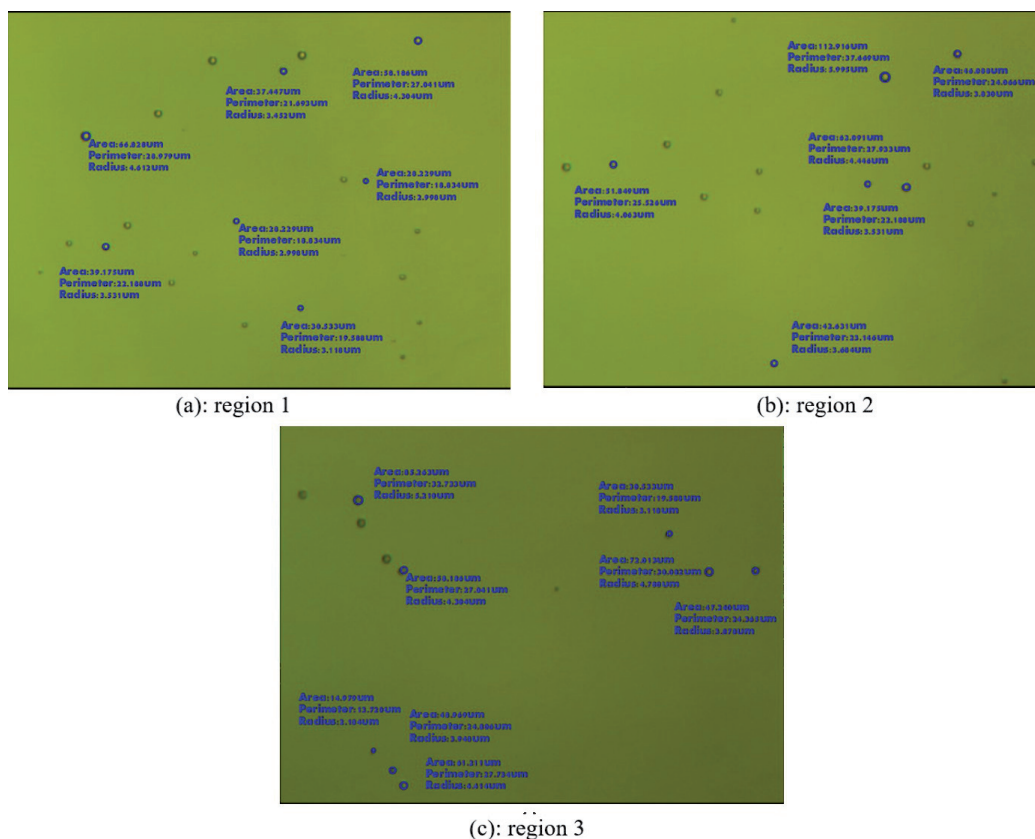


Fig. 3. Detecting images of three random regions in the concave pool of sampling piece.

Table 2. The radius and diameter of water-fog particles in the detecting images.

Region 1		Region 2		Region 3	
R [ $\mu\text{m}$ ]	D [ $\mu\text{m}$ ]	R [ $\mu\text{m}$ ]	D [ $\mu\text{m}$ ]	R [ $\mu\text{m}$ ]	D [ $\mu\text{m}$ ]
2.998	5.996	2.100	4.200	2.184	4.368
2.998	5.996	2.998	5.996	2.184	4.368
2.998	5.996	2.998	5.996	3.118	6.236
2.998	5.996	2.998	5.996	3.878	7.756
2.998	5.996	2.998	5.996	3.948	7.896
2.998	5.996	2.998	5.996	4.304	8.608
2.998	5.996	3.531	7.062	4.304	8.608
2.998	5.996	3.531	7.062	4.304	8.608
2.998	5.996	3.531	7.062	4.414	8.828
2.998	5.996	3.531	7.062	4.788	9.576
3.118	6.236	3.684	7.368	5.210	10.420
3.118	6.236	3.830	7.660	5.210	10.420
3.118	6.236	4.063	8.126	—	—
3.452	6.904	4.063	8.126	—	—
3.452	6.904	4.063	8.126	—	—
3.531	7.062	4.446	8.892	—	—
3.531	7.062	4.446	8.892	—	—
4.304	8.608	4.446	8.892	—	—
4.304	8.608	5.995	11.990	—	—
4.304	8.608	—	—	—	—
4.612	9.224	—	—	—	—

V of water fog flowing through the concave pool of sampling piece is calculated as  $2056148.6 \times 10^{-18} \text{ m}^3$ . Furthermore, the mass concentration of water-fog particles in the cross section of the spatial area where the collection point is located can be obtained as  $2.94 \times 10^{-4} \text{ g/m}^3$ .

#### Detection Comparison with Laser Particle Size Analyzer

The result of laser particle size analyzer for single nozzle spray are shown in Table 5 and Fig. 5. In the table, the corresponding data of D50 is  $8.78 \mu\text{m}$ . The particle size distribution curve is in good agreement with the detection results. The particle size distribution curve shifts about  $1.0 \mu\text{m}$ . With the intense particles collision in multi-nozzles spraying area, the water droplet size is slightly increased mostly due to agglomeration effect. The water fog less than  $10.0 \mu\text{m}$  is accessible to be drifted away, and the particle size of water fog will be decreased gradually due to evaporation, as well as the collection process. So the collection result at 10 m distance position from the spraying area was influenced.

#### Numerical Simulation Analysis of Particles Distribution

From the numerical calculation results, the airflow and the spray flow impact with each other on the front of the spray area. The location of the severe impact is related to the wind speed. The greater the wind speed, the more the position of the air interaction gradually moving back. The results from DPM calculation are pictured by particle tracking colored with particle size

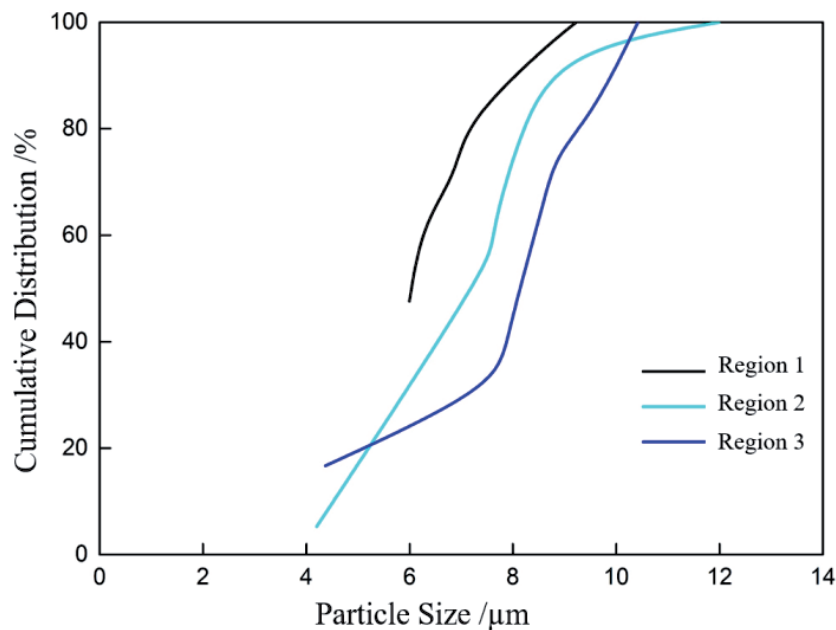


Fig. 4. Particle size distribution.

Table 3. Water-fog particles radius.

	$r_1$ [ $\mu\text{m}$ ]	$r_2$ [ $\mu\text{m}$ ]	$r_3$ [ $\mu\text{m}$ ]	$r_4$ [ $\mu\text{m}$ ]	$r_5$ [ $\mu\text{m}$ ]	$r_6$ [ $\mu\text{m}$ ]	$r_7$ [ $\mu\text{m}$ ]	$r_8$ [ $\mu\text{m}$ ]
(a)	3.00	3.12	3.45	3.53	4.30	4.61	—	—
(b)	2.10	3.00	3.53	3.68	3.83	4.60	4.45	6.00
(c)	2.18	3.12	3.88	3.95	4.30	4.41	4.79	5.21

Table 4. Number of water-fog particles.

	$n_1$ [pcs]	$n_2$ [pcs]	$n_3$ [pcs]	$n_4$ [pcs]	$n_5$ [pcs]	$n_6$ [pcs]	$n_7$ [pcs]	$n_8$ [pcs]
(a)	10	3	2	2	3	1	—	—
(b)	1	5	4	1	1	3	3	1
(c)	2	1	1	1	3	1	1	2

Table 5. Particle size distribution of laser particle size analyzer.

D50 [ $\mu\text{m}$ ]	D10 [ $\mu\text{m}$ ]	D25 [ $\mu\text{m}$ ]	D75 [ $\mu\text{m}$ ]	D90 [ $\mu\text{m}$ ]
8.78	5.86	7.56	9.69	10.70

and particle tracking colored with particle concentration in Fig. 6.

We can see that the particle size increases in the middle-rear part of the spray zone, and the particle size of the front and rear segments is small in speed of 0.5 m/s. And the distribution area of particle concentration is focused on the upper area in the latter part. In speed of 1.0 m/s, the particle size is below 8.0  $\mu\text{m}$  at the front part and increases slightly in the middle region. The particle size in the area between 30 m and 40 m increases gradually. Due to the increase of pressurized wind speed, the water-fog particles diffuse to the whole experimental tunnel rapidly. The concentration distribution of water-fog particles is uniform between 15 m and 40 m. The distribution gap between 40 m and 45 m is less uniform than the distribution in front-middle section. In speed of 1.5 m/s, the flow speed has

a great impact on the water-fog particles sprayed in the vertical direction. The water-fog particles are atomized completely due to the enhancement of external disturbance. Therefore, the length of the area with small particle size in the front section is lengthened, which delays the area with increased particle size in the middle section. The amount of water-fog particles is decreased, and the particle size distribution is less uniform than that at 1.0 m/s. So the phenomenon that water-fog particles cannot be collected may occur in the middle-rear section. In speed of 2.0 m/s, the water-fog particle size increases between 30 m and 40 m, and begins to decrease between 40 m and 50 m. The grain size distribution in the front region is similar to that in the spray zone at 1.5 m/s. At the distance from 20 m to 30 m to the air inlet surface, and from 35 m to 40 m, the particle distribution is high. The amount of particles in the middle section is small, whilst the amount of water droplets that can diffuse to the rear area is smaller.

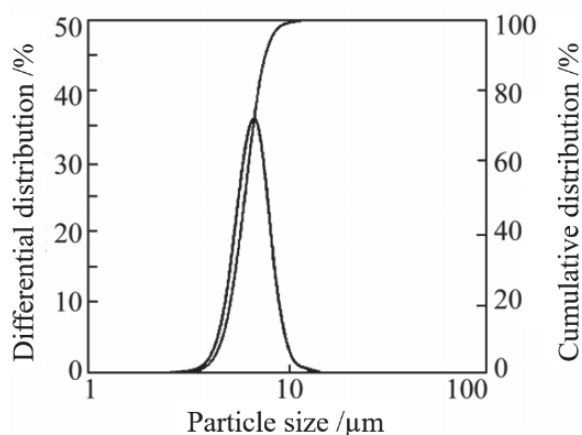


Fig. 5. Particle size distribution of laser particle sizer.

#### Field Experimental Analysis of Water-Fog Diffusion under Different Wind Speeds

From the particle diffusion in the experiments, the water fog is concentrated in the area below the nozzle. With the increase of spray amount, the water fog spreads to the surrounding area. After 2 min, the area below 1 m diffuses around and extends to 1~2 m along the ground. And 2 min later, the water fog below 1 m gradually accumulated upward and spread over 1 m.

As shown in Fig. 7, under the low wind speed of 0.5 m/s, the water-fog diffusion is stable for 5 min, and the visible distance is about 1 m. Due to the high concentration of water fog, water-fog particles can be

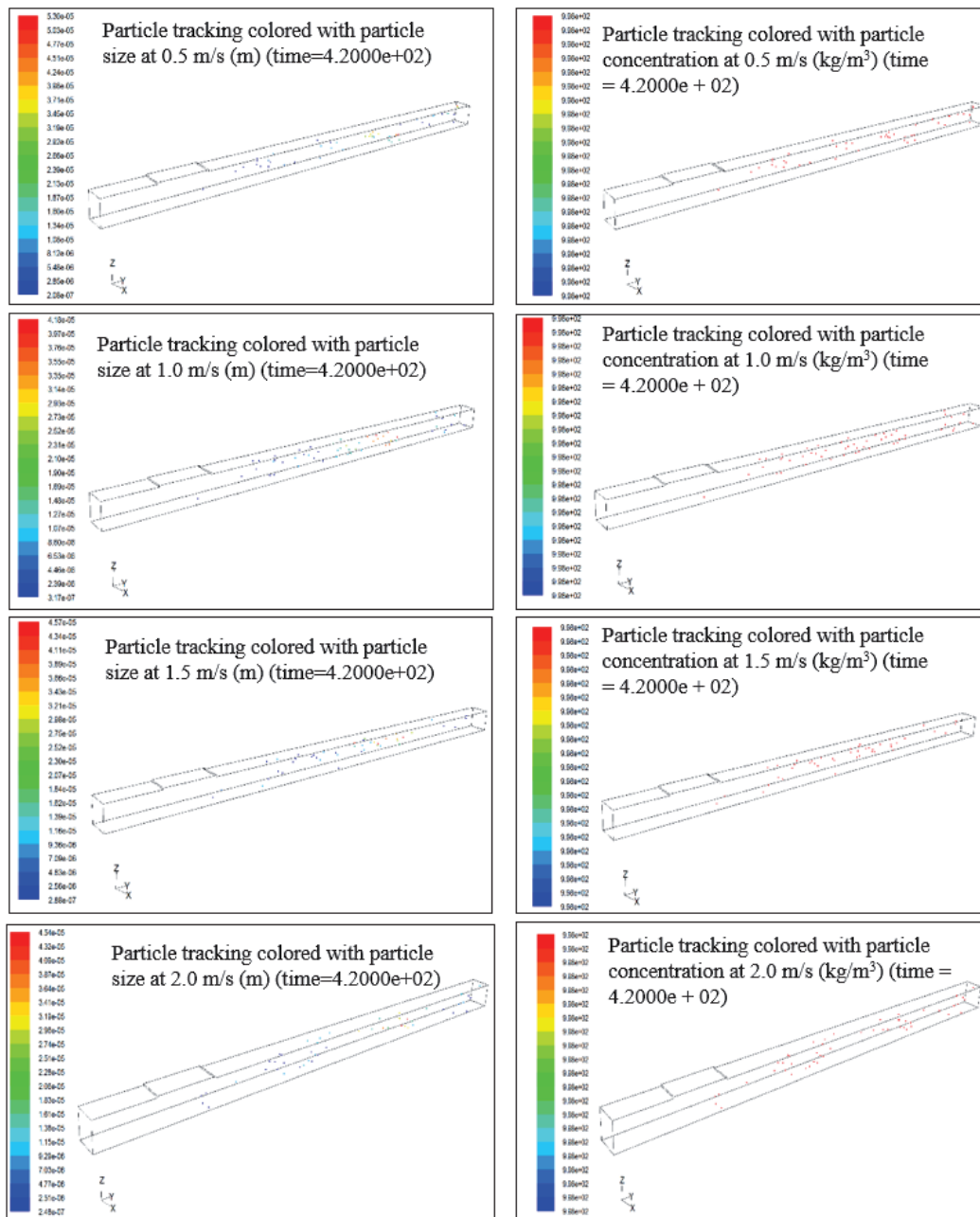


Fig. 6. Particles size and concentration distribution simulation result graphs under different wind speeds.

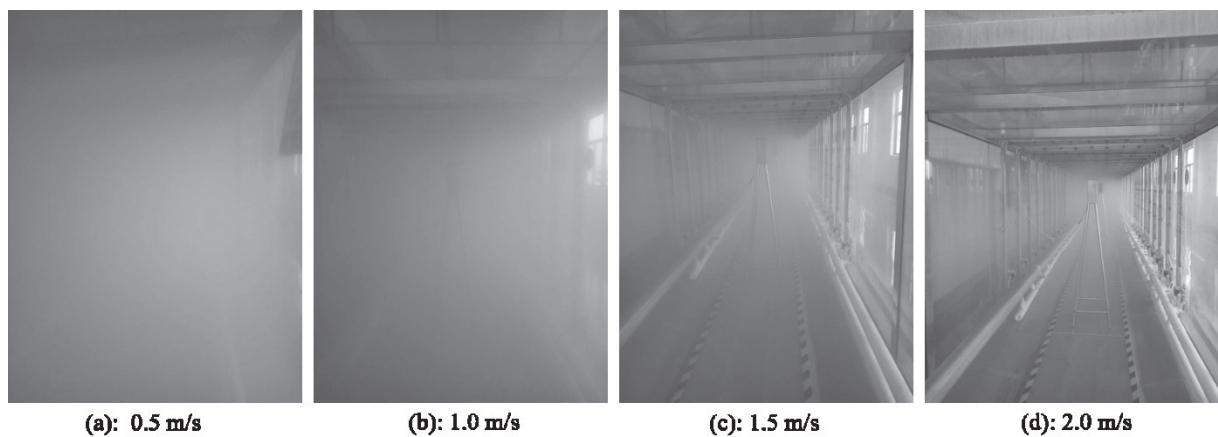


Fig. 7. Water-fog diffusion situations under different wind speeds.

collected at point 1 within 2 s. The water-fog diffusion time at 1.0 m/s is similar to that at 0.5 m/s, otherwise the water-fog concentration decreases slightly, and the visible distance is up to 2.0 m. The visual distance of 1.5 m/s has reached 10 m, and the water-fog concentration is low. The water-fog collection devices at 2.0 m/s are clearly visible in experimental tunnel. The collection of water-fog particles is more and more difficult with wind speed rise, and the collection time of water fog needs to be prolonged accordingly.

### Detection Experiments Results Analysis

According to the results in Fig. 8, in the condition of that the temperature is 24.2°C, whilst the humidity is 50% RH, while the wind speed in the experimental tunnel is 0.5 m/s and the spraying time is 2 min, the minimum particles diameter of No. 1 detecting point that can be clearly observed is 16.0 μm. The particle agglomeration is obvious in some areas, as well as No. 2, but the particle size of water fog that can be clearly observed is 10.0 μm below. The water agglomeration emerged in some areas, which has lost its statistical utility. The collected water-fog particles belonging to the transition zone of particle size reduction in the migration process couldn't be collected. In the condition of 24.5°C, 71% RH and 1.0 m/s, with the 3 min spraying, water-fog particles are

small in size but large in quantity at No. 3 and No. 4, which has influenced the statistical calculation. No. 5 and No. 6 belonging to the transition zone of water-fog particle size reduction also have no water-fog particles collected. From the 10 m to 30 m of spray zone, the particle size of water fog decreases gradually, and drops to 6.056 μm. The concentration of water fog gradually decreases within the range of 15 m from the spray zone, and the amount of water fog diffusing to the rear area also decreases. In the condition of 19.8°C, 50% RH and 1.5 m/s, with spray time 5 min, the values of water-fog particles size fluctuate from 5 m to 35 m in the spray zone, and the average particle size of water fog in the final collection area is quite small as low as 4.368 μm. The spray zone concentration of initial location is similar to that of 20 m, whilst the middle area of the spray decreases and picks up again. In the condition of 24.3°C, 49% RH and 2.0 m/s, with 3 min spraying, the water-fog concentration reaches the peak valley position in the 15 m distance from the spray area. The trend of water-fog particle size distribution is in accordance with its concentration distribution.

### Detection Technology Analysis

We can see that the designed particle collector can capture water-fog particles well in the space point area, with the functions of observing and analyzing

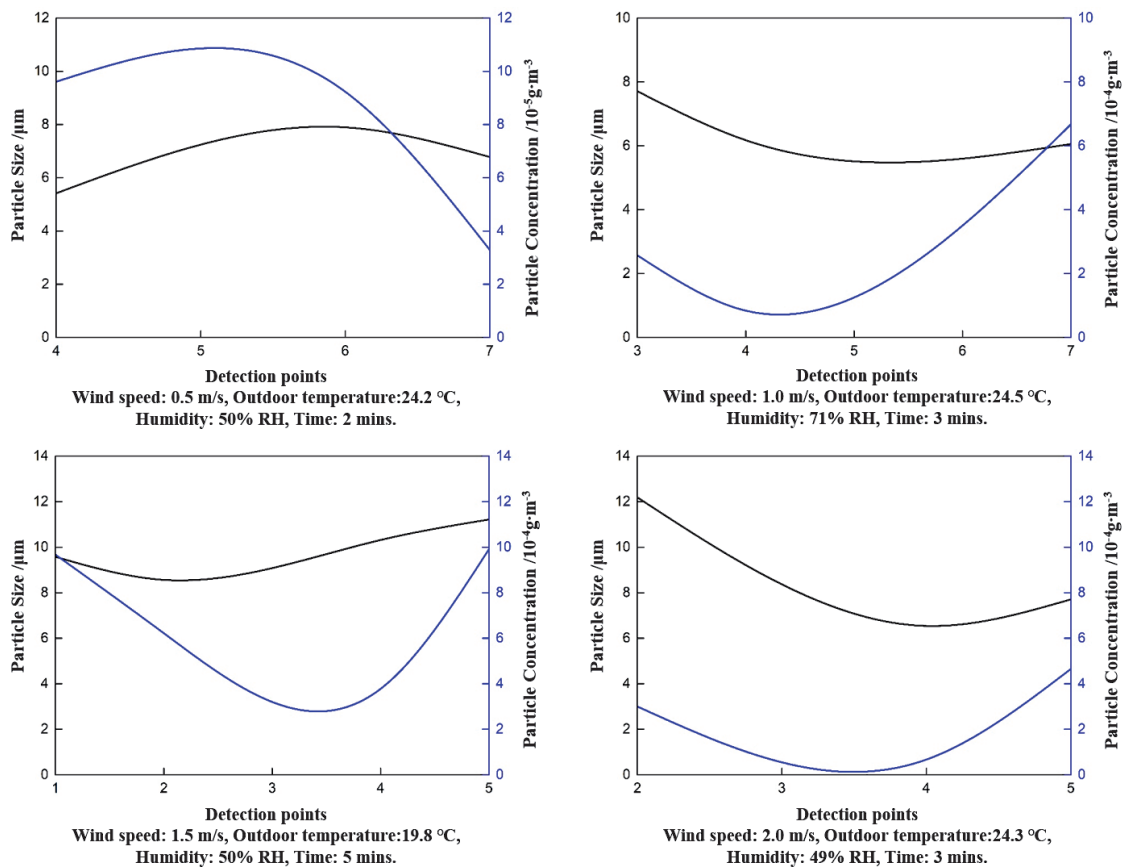


Fig. 8. Water-fog distribution in different conditions.

the particle morphology. Furthermore, three conclusions can be drawn here for reducing and avoiding errors from the process of experiments.

The amount of layers for water-fog particles in the concave pool should be controlled within two layers firstly. The water-fog particles are easy to penetrate the oil's outer surface as the small surface tension value. To make the sealing medium evenly spread in the sampling piece, the material of the sampling piece or its concave pool surface can be replaced by transparent and more corrosion-resistant material. The circumference of the rectangular concave pool can be set an inner fillet, or to change the concave pool into a circle directly with inner rounded corners all around. The thickness of the sealing medium in the concave pool determines the sampling effect and detection results, e.g., the tension, the density, the viscosity of the sealing medium, physical and chemical reaction with the sampling piece [29-32]. The water-fog particles should be effectively sealed by a kind of sealing medium with small fluidity. The impurities in the sealing medium should be reduced.

Secondly the short sampling time will increase the error of concentration calculation, and the longer sampling time will lead to the aggregation of water-mist particles [33]. These two situations of particle collection influence calculation precision. Determining the reasonable sampling time through experiments is quite essential with consideration of spray particle evaporation and agglomeration. For avoiding detection and calculation errors lastly, three-dimensional imaging equipment or plane imaging multi-directional imaging method can be considered.

## Conclusions

In this study, we independently explore and design a large space ultra-fine water-fog particle size and concentration detection technology, and a set of experimental system prototype, which can effectively obtain the large space multi-point water-fog particle size and concentration.

By spray flow field numerical simulation, from the detection points under different wind speed in the water-fog particle size and concentration of testing experiments with applying the new detection method, the results show that water-fog particle size distribution and the distance between the spray area is extended in the process of interaction with spray air, with the increase of pressure blast velocity. In the experimental tunnel, the particle size of water fog is risen in the middle section. Water-fog particle fault is appeared in the middle and rear section. The overall trend of water-fog particle size is decreased gradually, and the particle concentration is decreased first and then increased.

The generation and diffusion of water fog are quite unstable. Obtaining accurate rules through a large number of experiments, selecting a good measurement

method, and improving the detection technology and experimental system prototype according to good measurement method standards are necessary. Spray dust fall is also an unstable and random process. Therefore, finding and solving problems through experiments and improving the technology and experimental system comprehensively are essential.

## Nomenclature

$s'$	mm – concave pool area of the sample piece
$s''$	$\mu\text{m}$ – image area from metallographic microscope
$\rho$	$\text{kg}/\text{m}^3$ – fluid density
$v$	$\text{m}/\text{s}$ – fluid velocity
$P$	$\text{kg}/\text{m}^2$ – fluid pressure
$t$	s – time
$S$	$\text{kg}/\text{m}^3 \cdot \text{s}$ – source item
$\tau$	$\text{N}/\text{m}$ – shear force
$F$	$\text{N}/\text{m}^3$ – body force
$c_p$	$\text{w}\cdot\text{s}/\text{kg}\cdot\text{K}$ – constant pressure specific heat
$\lambda$	$\text{W}/\text{m}\cdot\text{K}$ – heat conductivity coefficient
$n$	$\text{pcs}$ – number of particles
$Q_r$	$\text{w}\cdot\text{s}/\text{m}^3$ – radiant heat
$J_{pK}$	$\text{N}/\text{m}^3$ – component force of the K - term particle diffusion flow
$F_{gpK}$	$\text{N}/\text{m}^3$ – resultant force of the particle on the fluid phase

## Acknowledgments

The authors are highly indebted to faculty members and laboratory staff of researching institutes for their support and cooperation during this research work.

## Conflict of Interest

The authors declare no conflict of interest with this research.

## References

1. HOSSEN M.A., CHOWDHURY A.I.H., MULLICK M.R.A., HOQUE A. Heavy metal pollution status and health risk assessment vicinity to Barapukuria coal mine area of Bangladesh. *Environmental Nanotechnology. Monitoring & Management*. **16**, 100469, **2021**.
2. LIU Q., PENG Y., LI Z., ZHAO P., QIU Z. Hazard identification methodology for underground coal mine risk management - Root-State Hazard Identification. *Resources Policy*. **72**, 102052, **2021**.
3. IJAZ M., AKRAM M., AHMAD S.R., KHAN W.U., THYGERSON S.M., NADEEM F.A. Dust Generation and respiratory impact of underground coal-producing mines in Pakistan. *Polish Journal of Environmental Studies*. **29**, (5), 3611, **2020**.
4. TONG R., CHENG M., YANG X., YANG Y., SHI M. Exposure levels and health damage assessment of dust

- in a coal mine of Shanxi Province, China. *Process Safety and Environmental Protection*. **128**, 184, **2019**.
5. FANG X., YUAN L., JIANG B., ZHU W., REN B., CHEN M., MU M., YU G., LI P. Effect of water–fog particle size on dust fall efficiency of mechanized excavation face in coal mines. *Journal of Cleaner Production*. **254**, 120146, **2020**.
  6. YIN W., ZHOU G., GAO D. Simulation analysis and engineering application of distribution characteristics about multi-stage atomization field for cutting dust in fully mechanized mining face. *Advanced Powder Technology*. **30**, (11), 2600, **2019**.
  7. YANG S., NIE W., LV S., LIU Z., PENG H., MA X., CAI P., XU C. Effects of spraying pressure and installation angle of nozzles on atomization characteristics of external spraying system at a fully-mechanized mining face. *Powder Technology*. **343**, 754, **2019**.
  8. LIU Z., NIE W., PENG H., YANG S., CHEN D., LIU Q. The effects of the spraying pressure and nozzle orifice diameter on the atomizing rules and dust suppression performances of an external spraying system in a fully-mechanized excavation face. *Powder Technology*. **350**, 62, **2019**.
  9. HU S., HUANG Y., FENG G., SHAO H., LIAO Q., GAO Y. Hu F., Investigation on the design of atomization device for coal dust suppression in underground roadways. *Process Safety and Environmental Protection*. **129**, 230-237, **2019**.
  10. CUI K., PANG X., ZHOU Z., REN Z. Efficient capture of fine particulate matters by ultrasonic atomization. *Journal of Environmental Chemical Engineering*. **9** (5), 106307, **2021**.
  11. DENG X., SUN S. Numerical investigation of impact breakage mechanisms of two spherical particles. *Powder Technology*. **364**, 954, **2020**.
  12. XIE Y., CHENG W., YU H., WANG Y. Study on spray dust removal law for cleaner production at fully mechanized mining face with large mining height. *Powder Technology*. **389**, 48, **2021**.
  13. WANG H., DU Y., WEI X., HE X. An experimental comparison of the spray performance of typical water-based dust reduction media. *Powder Technology*. **345**, 580, **2019**.
  14. LIU Y., CHENG L., SHEN Y., TIAN F., LIU H., SHI F. Size Distribution of Atmospheric Particulates and Pb concentrations in TSP during the cold-weather heating period. *Polish Journal of Environmental Studies*. **25** (1), 205, **2016**.
  15. SUN H., LUO Y., DING H., LI J., SONG C., LIU X. Experimental investigation on atomization properties of impaction-pin nozzle using imaging method analysis. *Experimental Thermal and Fluid Science*. **122**, 110322, **2021**.
  16. URBAN A., GRONIEWSKY A., MALY M., JOZSA V., JEDELSKY J. Application of big data analysis technique on high-velocity airblast atomization: Searching for optimum probability density function. *Fuel*. **273**, 117792, **2020**.
  17. GHASEMI A., LI X., HONG Z., YUN S. Breakup mechanisms in air-assisted atomization of highly viscous pyrolysis oils. *Energy Conversion and Management*. **220**, 113122, **2020**.
  18. ZHANG Y., YUAN S., WANG L. Investigation of capillary wave, cavitation and droplet diameter distribution during ultrasonic atomization. *Experimental Thermal and Fluid Science*. **120**, 110219, **2021**.
  19. KUHNHENN M., JOENSEN T. V., RECK M., ROISMAN I.V., TROPEA C. Study of the internal flow in a rotary atomizer and its influence on the properties of the resulting spray. *International Journal of Multiphase Flow*. **100**, 30, **2018**.
  20. XIA Y., KHEZZAR L., ALSHEHHI M., HARDALUPAS Y. Atomization of impinging opposed water jets interacting with an air jet. *Experimental Thermal and Fluid Science*. **93**, 11, **2018**.
  21. XIONG P., HE S., QIU F., CHENG Z., QUAN X., ZHANG X., LI W. Experimental and mathematical study on jet atomization and flash evaporation characteristics of droplets in a depressurized environment. *Journal of the Taiwan Institute of Chemical Engineers*. **123**, 185, **2021**.
  22. KIM K.D., JIN D.H., CHOI Y.C. Numerical simulation on the generation of ultrasound and formation of water fog in the ultrasonic gas atomizer. *Ultrasonics*. **102**, 105851, **2020**.
  23. HAN H., WANG P., LI Y., LIU R., TIAN C. Effect of water supply pressure on atomization characteristics and dust-reduction efficiency of internal mixing air atomizing nozzle. *Advanced Powder Technology*. **31** (1), 252, **2020**.
  24. SAEEDIPOUR M., SCHNEIDERBAUER S., PLOJL G., BRENN G., PIRKER S. Multiscale simulations and experiments on water jet atomization. *International Journal of Multiphase Flow*. **95**, 71, **2017**.
  25. YU H., JIN Y., CHENG W., YANG X., PENG X., XIE Y. Multiscale simulation of atomization process and droplet particles diffusion of pressure-swirl nozzle. *Powder Technology*. **379**, 127, **2021**.
  26. HUANG J., ZHAO X. Numerical simulations of atomization and evaporation in liquid jet flows. *International Journal of Multiphase Flow*. **119**, 180, **2019**.
  27. SHI G., LIU M., GUO Z., HU F., WANG D. Unsteady simulation for optimal arrangement of dedusting airduct in coal mine heading face. *Journal of Loss Prevention in the Process Industries*. **46**, 45, **2017**.
  28. QU X., REVANKAR S., QI X., GUO Q. Exploring on a three-fluid Eulerian-Eulerian-Eulerian approach for the prediction of liquid jet atomization. *Applied Thermal Engineering*. **195**, 117160, **2021**.
  29. HANNA R., ZOUGHAIB A. Atomization of high viscosity liquids through hydraulic atomizers designed for water atomization. *Experimental Thermal and Fluid Science*. **85**, 140, **2017**.
  30. VANKESWARAM S. K., DEIVANDREN S. Size and velocity characteristics of spray droplets in near-region of liquid film breakup in a swirl atomizer. *Experimental Thermal and Fluid Science*. **130**, 110505, **2022**.
  31. HAMMAD F.A., SUN K., CHE Z., JEDELSKY J., WANG T. Internal two-phase flow and spray characteristics of outside-in-liquid twin-fluid atomizers. *Applied Thermal Engineering*. **187**, 116555, **2021**.
  32. VEGAD C.S., KUMAR A., CHAKRAVARTHY S.R. Visualization of features of atomizing circular liquid sheet using simultaneous Volume Laser-Induced Fluorescence. *Experimental Thermal and Fluid Science*. **112**, 109947, **2020**.
  33. SHI Y., WEI J., QIU J., CHU H., BAI W., WANG G. Numerical study of acoustic agglomeration process of droplet aerosol using a three-dimensional CFD-DEM coupled model. *Powder Technology*. **362**, 37-53, **2020**.